

<https://cimav.repositorioinstitucional.mx/jspui/>

## **Microstructural properties of multi-nano-layered YSZ thin films**

P. Amézaga-Madrid, W. Antúnez-Flores, J. González-Hernández, J. Sáenz-Hernández, K. Campos-Venegas, O. Solís-Canto, C. Ornelas-Gutiérrez, O. Vega-Becerra, R. Martínez-Sánchez, M. Miki-Yoshida.

### **Abstract**

We report the fabrication of submicron, multi-nano-layered, yttria-stabilized zirconia (YSZ) thin films by aerosol assisted CVD. The film consisted of a periodic stack of several layers, a few nanometers thick, of the same composition but different density; formation of voids during synthesis originate the low-density layer. Grazing incidence X-ray diffraction (GIXRD), X-ray reflectometry, high-resolution transmission electron microscopy (HRTEM) and high angle annular dark field (HAADF) images were employed to analyze the microstructure of the films. GIXRD pattern showed characteristic peaks of cubic zirconia. Peak broadening in the pattern comes from a microstructure composed of nanocrystals, but principally due to the multilayered structure, that cause satellite peaks around the Bragg reflections. Lattice fringes measurement in HRTEM and HAADF images was consistent with the interplanar distance of the YSZ cubic phase. Additionally, lattice parameter obtained from selected area electron diffraction and GIXRD patterns was around 0.513 nm, in agreement to values reported in the literature for YSZ.

Keywords: Nanostructures, Thin films, Vapour deposition, Scanning and transmission electron, microscopy, X-ray diffraction.

## **Introduction**

Thin films of yttria-stabilized zirconia (YSZ) are important materials that exhibit exceptional properties, such as high chemical and mechanical stability, high electrical (electronic) resistivity, magnetic permittivity, low thermal conductivity, corrosion resistance, high ionic conductivity, and high refractive index [1]. Due to their properties, YSZ is used as electrolyte in solid oxide fuel cells [2,3], switchable mirrors [4], also in laser mirrors, optical coatings such as interference filters [5,6], and oxygen sensors [2]. On the other hand, multilayers films have been extensively used in soft X-ray optics, such as mirrors [7], optical devices [8], band pass filters, and beam splitters [9]. Many techniques have been employed to produce YSZ coatings including chemical vapor deposition [10] and variation of it such as aerosol assisted chemical vapor deposition (AACVD) [11], sol-gel [12], electron beam deposition [13], radio frequency and DC reactive magnetron sputtering [14], as well as reactive evaporation [15]. Among these techniques, AACVD has proved to be a simple, reproducible and inexpensive method to produce metallic oxide thin films.

In this work, we report the fabrication of submicron, multinano-layered, YSZ thin films by AACVD. Grazing incidence X-ray diffraction (GIXRD), X-ray reflectometry (XRR), high-resolution transmission electron microscopy (HRTEM) and high angle annular dark field (HAADF) techniques were employed to analyze the microstructure of the films.

## **Experimental**

Y stabilized  $ZrO_2$  thin films were deposited onto borosilicate (2.5cm×7.5 cm) glass substrates by AACVD technique, details of the experimental set up have been

<https://cimav.repositorioinstitucional.mx/jspui/>

described before [16]. The starting solution was a dilution of Zr acetylacetonate ( $0.083 \text{ mol dm}^{-3}$ ) and Y acetate ( $0.017 \text{ mol dm}^{-3}$ ) in methanol (99.9% pure). Substrate temperature was fixed to the optimum value of  $723 \pm 5 \text{ K}$ . The carrier gas was micro-filtered air at the optimized pressure of 310 kPa and fluxes of  $5 \text{ L min}^{-1}$ . The aerosol, generated by an ultrasonic nebulizer and carried by the air, was directed towards the substrate by a nozzle, which has a periodic movement at constant velocity to scan the whole surface of the substrate. One scan is equivalent to one deposition step. Samples E and F were obtained with particular conditions, in order to analyze its influence on the growth characteristics of the film. Sample E was deposited including five dual sequences of one deposition step followed by 5 min of stand-by without spraying. In contrast, sample F was obtained in five sequences of one deposition step with  $5 \text{ L min}^{-1}$  followed by a second one with  $1 \text{ L min}^{-1}$ . Carrier gas flux of  $1 \text{ L min}^{-1}$  was used to generate a cloud of aerosol precursor that did not impinge directly onto the substrate. Table 1 presents the principal preparation parameters of the samples analyzed in this report.

Crystalline structure of the samples was analyzed by grazing incidence XRD in a Pan-analytical X-Pert system, the patterns were obtained using Cu K $\alpha$  radiation at 40 keV and 30 mA. Diffracted beam path included a graphite flat crystal monochromator. Grazing incidence angle was fixed at  $0.5^\circ$ ; whereas the scanning angle  $2\theta$  was varied between  $25^\circ$  and  $80^\circ$ , at  $0.02^\circ$  step. Surface morphology and crosssectional microstructure of the films were studied by field emission SEM using a JEOL JSM-7401F. Cross-sectional samples were also studied by TEM. High-resolution transmission electron microscopy (HRTEM), and related techniques were performed in

<https://cimav.repositorioinstitucional.mx/jspui/>

a JEOL JEM-2100F with beam Cs-corrector, operated at 200 kV. For cross-section studies, SEM samples were prepared by conventional methods in a cross-section polisher JEOL SM-09010 operated at 5 kV and 120  $\mu$ A. In addition, TEM cross-section samples were prepared using a focused ion beam (FIB) JEOL JEM-9320 system operated at 30 kV. Elemental analysis of the films was achieved by means of energy dispersive X-ray spectroscopy (EDS), using an Inca Microanalysis System attached to the electron microscope.

**Table 1**  
Principal preparation parameters of the films analyzed in this report.

Sample	Deposition time (min)	Steps	Distance nozzle-substrate (cm)	Section of nozzle (cm <sup>2</sup> )	Velocity of nozzle (mm s <sup>-1</sup> )	Thickness (nm)	Thickness dense layer (nm)	Thickness porous layer (nm)
A	19	15	3	1.05	0.4	160	5	15
B	38	30	1	1.77	0.4	530	10	9
C	30	20	3	1.05	0.4	71	–	–
D	98	19	1	1.77	0.1	293	–	–
E <sup>a</sup>	13	5	1	0.76	0.1	190	8	20
F <sup>b</sup>	27	10	1	0.76	0.1	51	6	5

<sup>a</sup> Sample E does not include in its deposition time, 4 intervals of 5 min of stand-by without spraying, between each deposition step.

<sup>b</sup> Sample F was deposited in 5 pair sequences of one deposition step with 5 L min<sup>-1</sup> and other with 1 L min<sup>-1</sup>.

## Results and discussion

Film characteristics and composition: The film consisted of a periodic stack of several YSZ layers, a few nanometers thick, of the same composition but different density, the low-density layer being present due to the existence of voids. The multilayered microstructure is shown in cross-sectional HAADF STEM (Fig. 1a and b) and backscattered SEM (Fig. 1c and d) micrographs. Fig. 1a shows an overview of the cross-section of sample B. Fig. 1b presents an atomic resolution Z-contrast image of sample B, showing the high density and porous layers. Backscattered SEM micrograph of sample E (Fig. 1c) shows again several dense/porous layers formed during the repeated dual sequence deposition step/stand-by. In addition, sample F (see Fig. 1d)

<https://cimav.repositorioinstitucional.mx/jspui/>

also display several dense/porous layers deposited during the repeated deposition steps of  $5/1 \text{ Lmin}^{-1}$ .

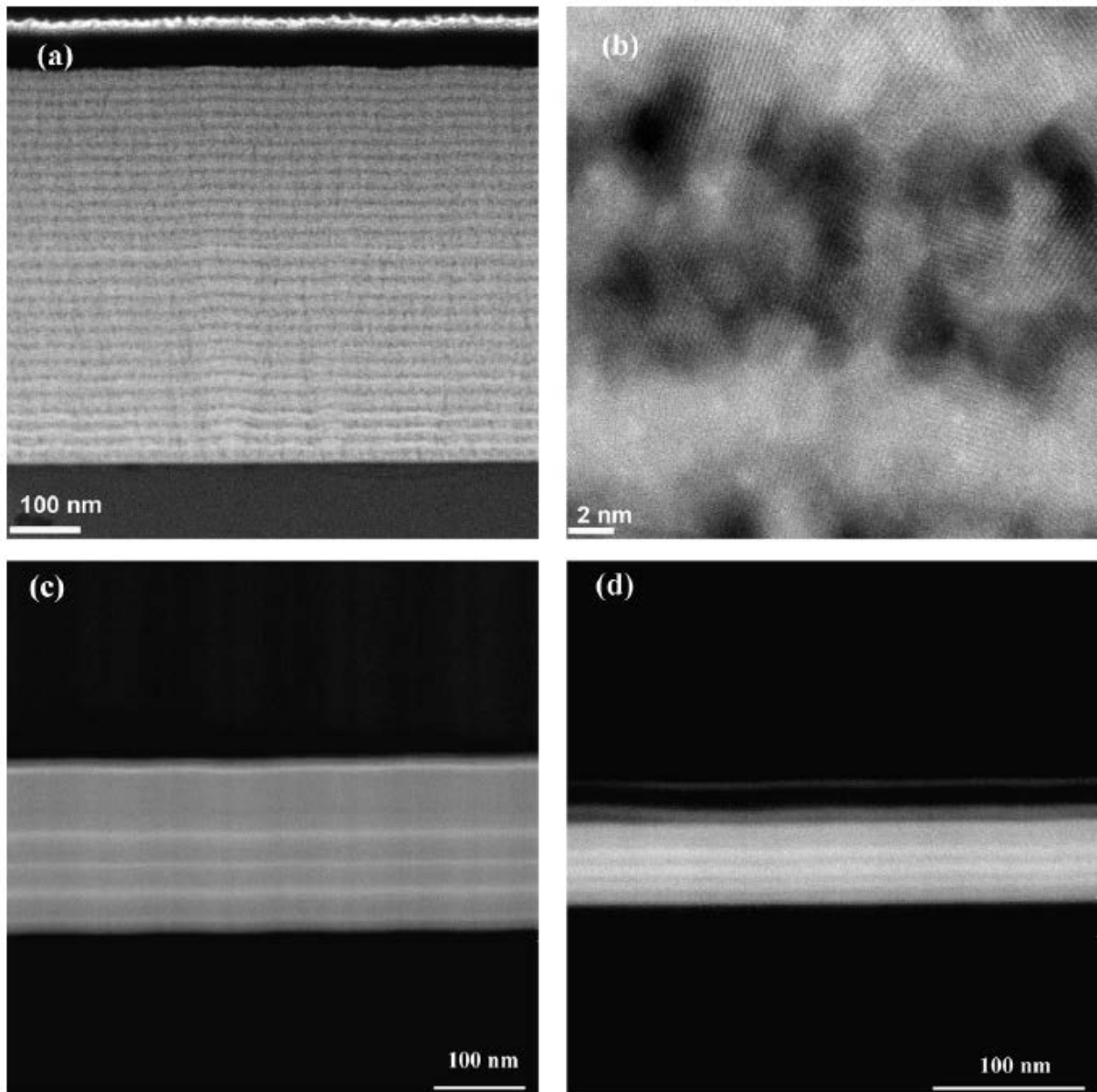


**Fig. 1.** HAADF STEM images of sample B. (a) Overview of the cross-section, (b) Atomic resolution Z-contrast image showing the dense and porous layers. Backscattered SEM images (c) sample E and (d) sample F.

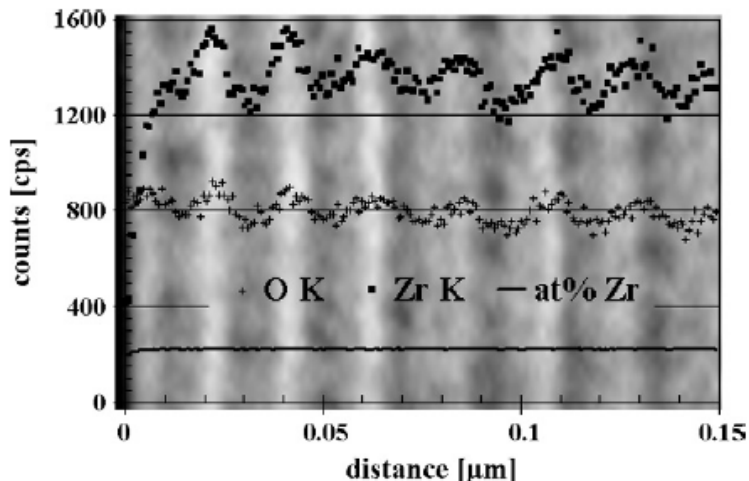


**Fig. 2.** Line scan EDS analysis of several layers superposed to HAADF images. Maxima counts of O K and Zr K lines coincide with bright (dense) zones of the image (sample). In contrast at.% of Zr is almost constant, indicating uniform composition of the film.

The number of layers matches with the number of spraying steps during the deposition. In Table 1 they also tabulated the thickness of the films and the average thickness of dense and porous layers.

The composition of the films was studied by EDS. The analysis showed that Zr and Y in the film were almost in the same proportion than in the started solution (mol ratio Y/Zr~0.20). EDS line scanning was performed across several layers on a TEM cross-section of sample B, to verify the composition homogeneity of the films. Fig. 2 shows a Z-contrast image superimposed to EDS results. Maxima of EDS counts of different elements (Zr, O, and Y) coincide with bright (dense) zones of the sample (Y not shown for clarity). In contrast at.% of Zr and Y are almost constant along the scanned line. This result strongly supports the fact that the composition of all the layers is the same.

<https://cimav.repositorioinstitucional.mx/jspui/>

Microstructure: Fig. 3 shows the grazing incidence X-ray diffraction pattern of films analyzed in this work; they showed characteristic XRD peaks of cubic YSZ phase [17]. No phase segregation into  $Y_2O_3$  or other metallic elements was observed. Peak broadening in the pattern indicates a microstructure composed of nanocrystals, which were also observed in HRTEM (see Fig. 4) and HAADF images (Fig. 1b). However, the principal contribution to the peak broadening was the satellite peaks around the Bragg reflection, due to the multilayered structure of the film [18]. The position of the  $m$ th order satellite peak ( $\theta_{\pm}$ ) can be obtained from:

$$\sin(\theta_{\pm}) = \sin(\theta_B) \pm \frac{m\lambda}{2p}$$

where  $\theta_{\pm}$  is the position of  $m$ th positive or negative satellite peak,  $\theta_B$  is the Bragg reflection position,  $\lambda$  is the X-ray wavelength, and  $p$  the period of the multilayer [18]. In our case, for a period in the range of 20 nm, and the Bragg reflection between  $15^\circ$  and  $40^\circ$ , calculated first order satellite peak are around  $0.22$ – $0.29^\circ$ . The Bragg angles were determined for the most intense reflections and an average lattice parameter of  $0.512 \pm 0.001$  nm was deduced, close to values reported in the literature [19]. A slight tendency to increase the lattice parameter and the full-width at half-maximum (FWHM) of the (1 1 1) reflection with the thickness of the films was observed, probably due to an increase of the stress in the films caused by the difference in expansion coefficients of the film and substrate.

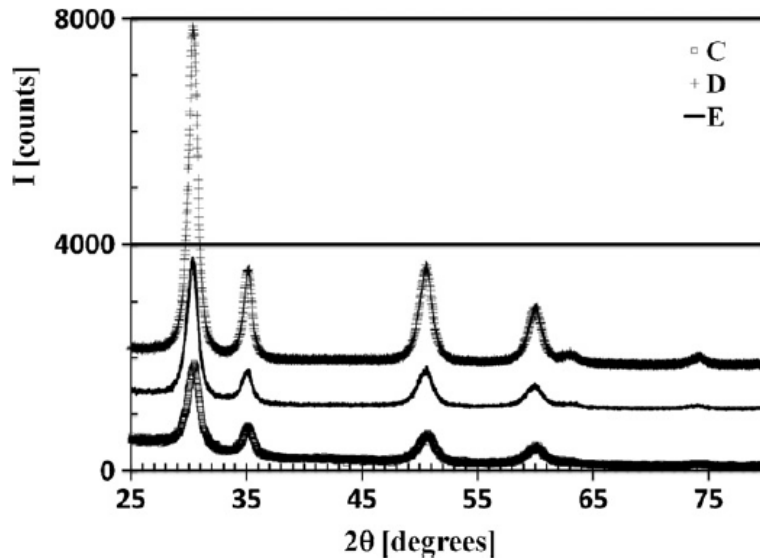


Fig. 3. GIXRD pattern of representative samples. Lattice parameter of  $0.512 \pm 0.001$  nm was deduced from these patterns.

It is worthwhile to remark that very well crystallized nanometric grains constituted the films, as it is shown in the HRTEM micrograph of sample A in Fig. 4. Lattice fringes measurement in Figs. 1b and 4 was consistent with the interplanar distance of the YSZ phase [17].

Moreover, selected area electron diffraction patterns results also confirm the existence of the stabilized phase (see inset of Fig. 4). The lattice parameter obtained from SAED patterns was  $0.514 \pm 0.005$  nm, in agreement to values reported in the literature [19] for cubic zirconia. To verify that the crystalline structure of the layers is the same; nanobeam diffraction was performed in individual layers of sample B. Fig. 5a shows a bright field TEM micrograph indicating the positions of the nanobeam (1 and 3) onto the sample. The nanobeam diameter on the surface of the film was estimated around 50 nm. NBD patterns of a dense layer (Beam 1) and porous layer (Beam 3) are shown in Fig. 5b and c, respectively. Both patterns present the same rings and overall

<https://cimav.repositorioinstitucional.mx/jspui/>

characteristics, similar to the SAED pattern of Fig. 4. Differences of intensity in the spots were caused by differences in density of the layers; dense layers give more intense spots in the pattern.

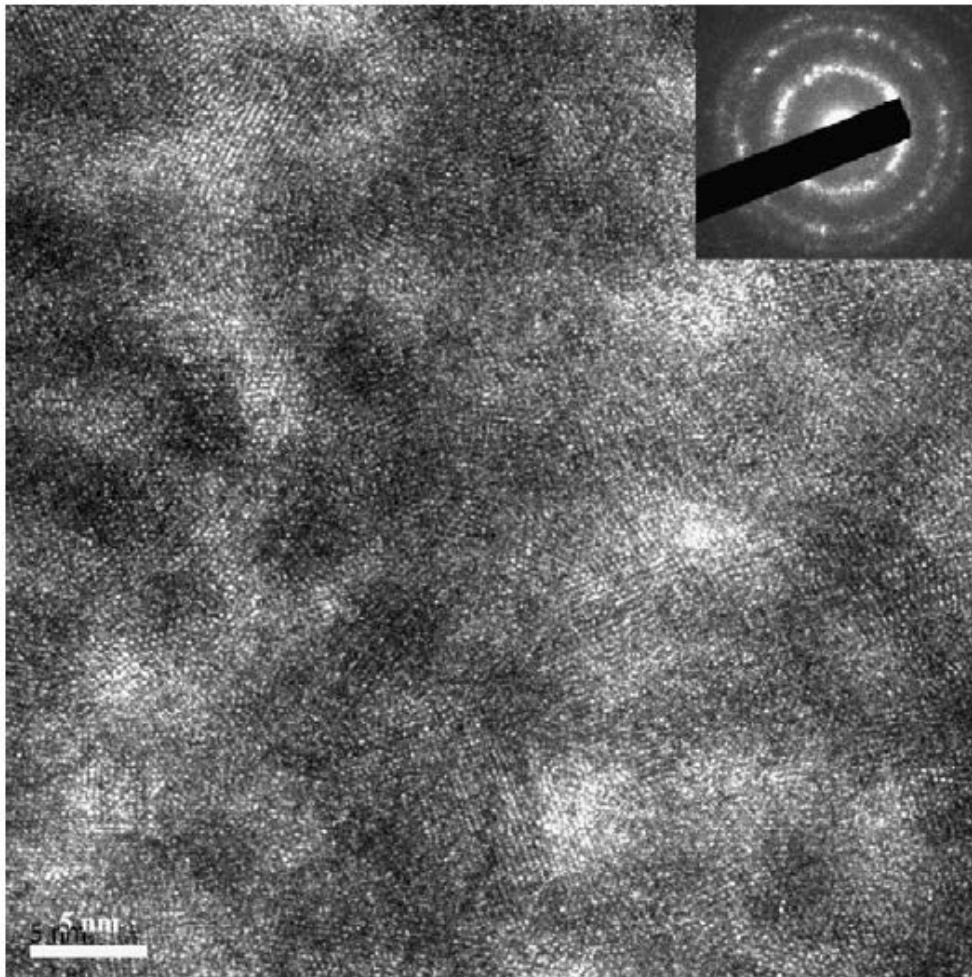


**Fig. 4.** HRTEM micrograph of sample A. Inset shows its SAED pattern.

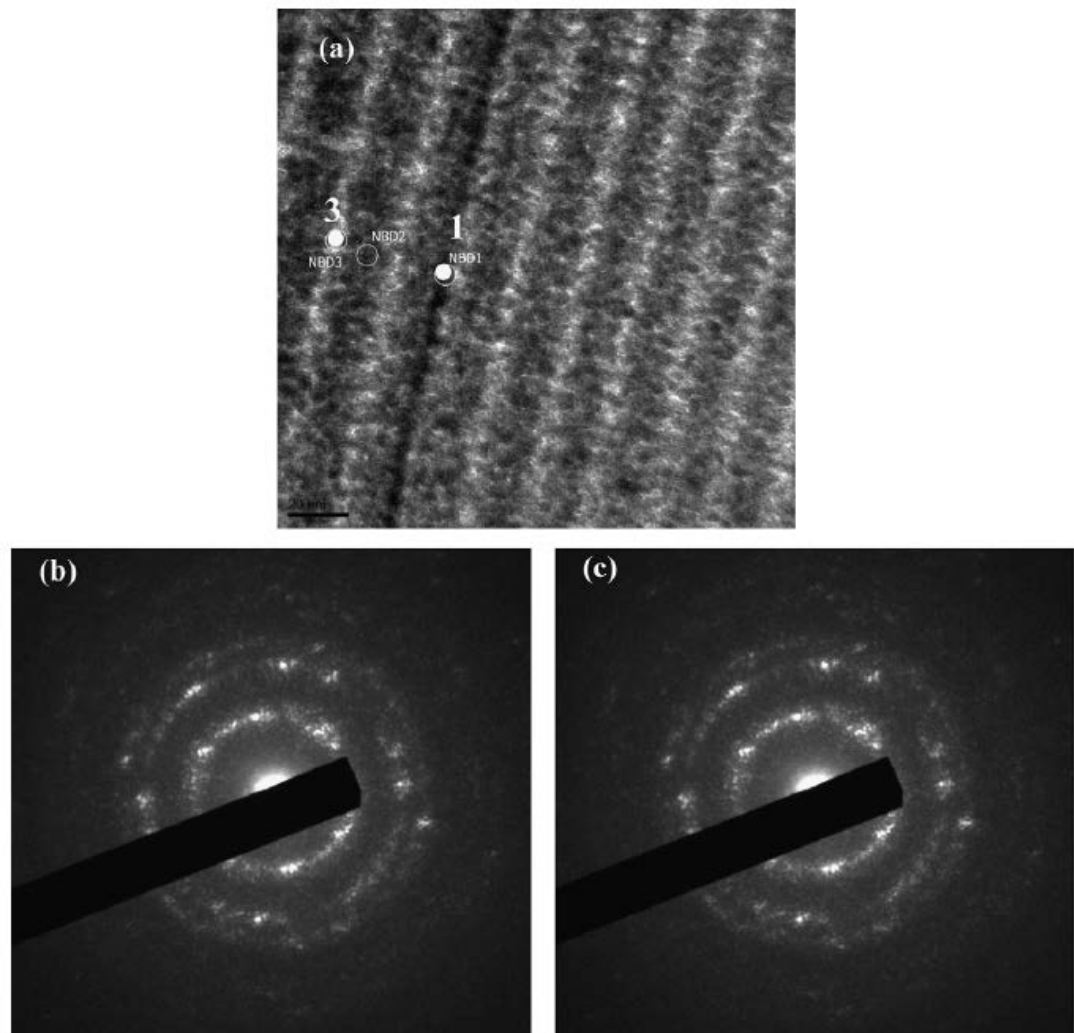


**Fig. 5.** (a) Bright field image showing the area of analysis, and the two positions for the nanobeam. (b and c) NBD patterns of a dense layer (Beam 1) and porous layer (Beam 3), respectively.

X-ray reflectometry was performed on several films. Fig. 6 shows typical XRR pattern of sample C. It is shown that several modulations due to the films thickness, indicating very good homogeneity and smooth interfaces; in addition, other modulation (see arrow in Fig. 6) observed around  $0.85^\circ$  can be associated with multilayered

<https://cimav.repositorioinstitucional.mx/jspui/>

structure. The observed peaks occur at positions of  $2\theta$  given by a modified form of Bragg's law [20]:

$$\sin^2(\theta) = \left(\frac{m\lambda}{2p}\right)^2 + 2\delta$$

where  $m$  is the order of the reflection,  $\lambda$  is the X-ray wavelength,  $p$  is the period in the multilayer, and  $S$  is the real part of the average refractive index of the film. By plotting  $\sin^2 \theta$  vs  $m^2$  and fitting to a straight line,  $p$  can be determined very accurately from the slope of the line. The  $2S$  term represents the refraction of X-rays within the film. From the XRR pattern of film C, it was calculated a film thickness of 75 nm, very close to that determined by optical methods (see Table 1). Parameter  $\iota$  was also calculated around  $6.2 \times 10^{-6}$ . The modulation observed around  $0.85^\circ$ , can be associated with a multilayer period of  $13 \pm 3$  nm.

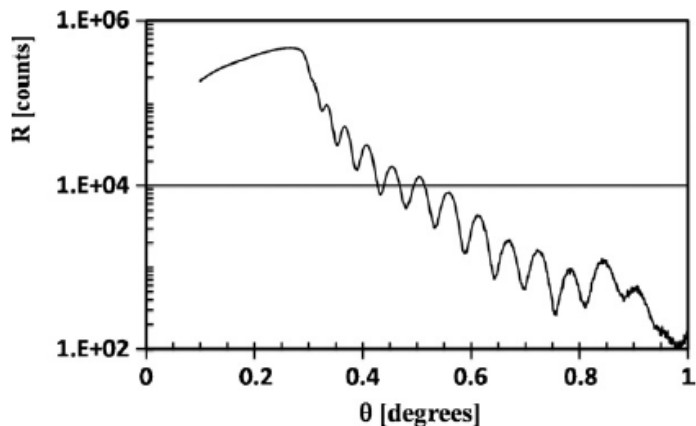


**Fig. 6.** XRR pattern of sample C. It is shown that modulations in the reflected signal are due to film thickness. The arrow shows the position of other peak that is correlated with the multilayered structure.

## Conclusions

<https://cimav.repositorioinstitucional.mx/jspui/>

Multi-nano-layered yttria-stabilized zirconia thin films were deposited by aerosol assisted CVD. The film consisted of a periodic stack of several YSZ layers, a few nanometers thick, of the same composition but different density, the low-density layer being present due to the existence of voids. All the experimental evidence: line scan microanalysis by energy dispersive spectroscopy, high-resolution transmission electron microscopy, high angle annular dark field STEM, selected area electron diffraction (SAED), and nanobeam diffraction suggested that the layers have the same composition but different density. Analysis by X-ray diffraction indicates the presence of a cubic YSZ phase, consistent with results of SAED patterns, HRTEM and HAADF images analysis. X-ray reflectometry results indicated very good homogeneity of the films and smooth interfaces.

### **Acknowledgements**

The authors would like to thank E. Torres, S. Miranda, M. Moreno, for their technical assistance. We are in debt with Application Lab. JEOL for cross-section preparation, SEM and HAADF analysis. Also to Application Lab. FEI for FIB preparation. This work was partially supported by a grant from CONACYT-SEP 47911.

### **References**

- [1] G. Laukaitis, J. Dudonis, D. Milcius, *Vacuum* 81 (2007) 1288–1291.
- [2] M.F. García-Sánchez, J. Peña, A. Ortiz, G. Santana, J. Fandiño, M. Bizarro, F. Cruz-Gandarilla, J.C. Alonso, *Solid State Ionics* 179 (2008) 243–249.
- [3] C.D. Baertsch, K.F. Jensen, J.L. Hertz, H.L. Tuller, S.T. Vengallatore, S.M. Spearing, M.A. Schmidt, *J. Mater. Res.* 19 (2004) 2604.
- [4] A.L. Larsson, A. Gunnar, A. Niklasson, *Sol. Energy Mater. Sol. Cells* 84 (2004)

<https://cimav.repositorioinstitucional.mx/jspui/>

351–360.

[5] S. Venkataraj, O. Kappertz, H. Weis, R. Drese, R. Jayavel, M. Wuttig, *J. Appl. Phys.* 92 (2002) 599–607.

[6] W.H. Lowdermilk, D. Milam, F. Rainer, *Thin Solid Films* 73 (1980) 155–166.

[7] J. González-Hernández, B.S. Chao, S.R. Ovshinsky, D.D. Allred, *J. X-ray Sci. Technol.* 6 (1996) 1–31.

[8] M. Ghanashyam Krishna, A.K. Bhattacharya, *Mater. Sci. Eng. B* 86 (2001) 41–47.

[9] D. Bhattacharyya, N.K. Sahoo, S. Thakur, N.C. Das, *Vacuum* 60 (2001) 419–424.

[10] K.L. Choy, *Prog. Mater. Sci.* 48 (2003) 57–170 (and references there in).

[11] M. Miki-Yoshida, F. Paraguay-Delgado, W. Estrada-Lopez, E. Andrade, *Thin Solid Films* 376 (2000) 99–109.

[12] J. Zhang, L. Gao, *J. Solid State Chem.* 177 (2004) 1425.

[13] S. Ramamurthy, N.S. Subramanian, K. Sarangarajan, B. Santhi, *Bull. Electrochem.* 14 (1998) 446.

[14] P.F. Carcia, R.S. McLean, M.H. Reilly, Z.G. Li, L.J. Pillione, R.F. Messier, *J. Vac. Sci. Technol. A* 21 (2003) 745.

[15] J. Philip, N. Theodoropoulou, G. Berera, J.S. Moodera, B. Satpati, *Appl. Phys. Lett.* 85 (2004) 777.

[16] P. Amézaga-Madrid, W. Antúnez-Flores, I. Monárrez-García, J. González-Hernández, R. Martínez-Sánchez, M. Miki-Yoshida, *Thin Solid Films* 516 (2008) 8282–8288.

[17] Joint Committee on Powder Diffraction Standards, *Powder Diffraction File*,



<https://cimav.repositorioinstitucional.mx/jspui/>

International Center for Diffraction Data, Swarthmore, PA, 2008, card 00-30-1468.

[18] C. Ducros, C. Cayron, F. Sanchette, Surf. Coat. Technol. 201 (2006) 136.

[19] B. Butz, P. Kruse, H. Störmer, D. Gerthsen, A. Müller, A. Weber, E. Ivers-Tiffée, Solid State Ionics 177 (2006) 3275.

[20] P.C. Yashar, W.D. Sproul, Vacuum 55 (1999) 179.

